ChemSusChem

Research Article
doi.org/10.1002/cssc.202402325

Chemistry Europe
European Chemical Societies Publishing

www.chemsuschem.org

Stable Na^+ Ion Storage via Dual Active Sites Utilization in Covalent Organic Framework-Carbon Nanotube Composite

Anupam Dey[+],[a] Atin Pramanik[+],[b] Sougat Purohit,[c] Sandip Biswas,[a] Shreyasi Chattopadhyay,[b] Tymofii S. Pieshkov,[b, d] Gopalakrishnan Sai Gautam,[c] Pulickel M. Ajayan,*[b] and Tapas Kumar Maji*[a]

Redox-active covalent organic frameworks (COFs) with metal binding sites are increasingly recognized for developing cost-effective, eco-friendly organic electrodes in rechargeable energy storage devices. Here, we report a microwave-assisted synthesis and characterization of a triazine-based polyimide **COF** that features dual redox-active sites (−C=O from pyromellitic and −C=N− from triazine) and **COF@CNT** nanocomposites (**COF@CNT-X**, where X = 10, 30, and 50 wt% of NH_2-MWCNT) formed through covalent linking with amino-functionalized multiwalled carbon nanotubes. These composites are evaluated as cathode materials for the sodium-ion batteries (SIBs). The amine functionalization renders the covalent bond between **COF** and CNT, improving electronic conductivity, structural rigidity, and long-term stability. The interfacial growth of **COF** layers on CNTs increases accessible redox-active sites, enhancing sodium diffusion kinetics during sodiation/desodiation. The **COF@CNT-50** composite exhibits outstanding Na^+ ion storage performance (reversible capacity of 164.3 mAh g^{-1} at 25 mA g^{-1}) and excellent stability over 1000 cycles at ambient temperature. At elevated temperature (65 °C), it also maintains good capacity and cycle stability. *Ex situ* XPS analysis confirms the importance of dual active sites in the Na^+ diffusion mechanism. Density functional theory (DFT) calculations reveal insights into Na^+ binding sites and corresponding binding energies into **COF** structure, elucidating the experimental storage capacity and voltage profile.

1. Introduction

The development of innovative and reliable electrochemical energy conversion and storage technologies is recognized as an urgent need to combat the overuse of fossil fuels and the steady growth of global energy demand.[1–5] In the context of electric energy storage and utilization, sodium-ion batteries (SIBs) have recently emerged as an alternative to the market-dominant LIBs, owing to abundant resources, wide distribution, and much cheaper ingredients than lithium.[6–10] As the performance of SIB largely depends upon the electrode materials, several efforts have been made to develop suitable electrode materials.[11–13] Presently, sodium-containing transition metal oxides or polyanions (provide the redox centre) act as typical cathode materials for SIBs.[14] However, fabricating these inorganic materials is always expensive, energy-intensive, and environmentally unfriendly.[15–17] Comparatively, organic materials have many benefits, such as low cost, excellent structural tunability, non-toxic, and lightweight, making them potent next-generation energy storage electrode materials.[18–20] As a result, various redox-active organic materials have been tested in electrodes, including organic radical compounds,[21–23] carbonyl compounds,[24–25] organosulfur compounds,[26–27] and azo compounds.[28] However, small organic molecules suffer from low intrinsic electric conductivity, solubility in aprotic electrolytes, and minimal redox stability. A successful tactic is to attach redox-active organic molecules to a polymeric framework and increase their stability.[29–30] But, most of the conducting organic polymers are nonporous in nature. This results in inefficient access of redox-active centers by ions or electrons. Additionally, it causes slow transportation of electrolytes, which leads to low efficiency, especially at high rates.[31–32] Therefore, developing two- or three-dimensional (2D or 3D) porous polymers with redox-active units can be considered an important strategy to address the challenges mentioned with organic electrode materials.[33–35]

In this perspective, covalent organic frameworks (COFs), a class of crystalline, porous organic polymers with various redox-active sites, have received significant attention in developing effective organic electrode materials.[36–37] The characteristics of open porous channels, robust π-conjugated and strong covalent network in COF, can facilitate faster ion/electron trans-

[a] *Molecular Materials Laboratory, Chemistry and Physics of Materials Unit (CPMU), School of Advanced Materials (SAMat), International Centre for Materials Science (ICMS), Jakkur, Jawaharlal Nehru Centre for Advanced Scientific Research, Bangalore, India*
[b] *Department of Material Science and NanoEngineering, Rice University, Houston, United States*
[c] *Department of Materials Engineering, Indian Institute of Science, Bangalore, India*
[d] *Applied Physics Graduate Program, Smalley-Curl Institute, Rice University, Houston, United States*

Correspondence: *Tapas Kumar Maji, Molecular Materials Laboratory, Chemistry and Physics of Materials Unit (CPMU), School of Advanced Materials (SAMat), International Centre for Materials Science (ICMS), Jakkur, Jawaharlal Nehru Centre for Advanced Scientific Research, Bangalore 560064, India.*
Email: tmaji@jncasr.ac.in

Pulickel M. Ajayan, Department of Material Science and NanoEngineering, Rice University, Houston TX-77005, United States.
Email: ajayan@rice.edu

[+] *Contributed equally.*

Supporting Information for this article is available on the WWW under https://doi.org/10.1002/cssc.202402325

portation over an extended period.[34,38–43] However, most COFs currently known to exist in SIB have a single redox active group (either −C=O or −C=N− unit), which invariably results in low output capacity.[44] To attenuate this issue, designing COFs with multiple redox active sites can enhance the output capacity effectively. In this context, the design and synthesis of triazine-based polyimide COFs can be an excellent choice for achieving higher energy storage performance.[45] The incorporation of both −C=N− (from triazine moiety) and −C=O groups (from imide moiety) in the triazine-based polyimide COFs can function as dual redox active cathode material since the strong electronegative 'O' and 'N' atoms will be accessible to interact with the cations during reversible charging and discharging process.[44,46] Furthermore, pristine-bulk COF electrodes are also constrained with low electrochemical energy storage performance by poor electrical conductivity and lower utilization of active sites.[47–48] A potential solution to this bottleneck is constructing COF-composite material by growing a few layers of COF interfacially on top of a conductive additive, like graphene or carbon nanotubes (CNTs). There are few previous reports where, after the integration of CNT into a covalent polymer framework, higher electrochemical performance was obtained.[46,49–50] However, earlier reports majorly discussed the integration of CNT with the COF by weak Van der Waals interaction, which can occasionally impair the material's long-term stability, diffusion of ions, and electrical conductivity rate. Therefore, the covalent linkage between COFs and CNTs emerges as a compelling approach to boost the electrochemical performance of electrodes.[48] Additionally, the reported composite organic electrode materials have only been tested at ambient temperature (25 °C). However, in the deserts and tropical regions, a high-temperature working range is essential for the practical applications of rechargeable batteries.[51–52] Unfortunately, achieving reliable battery performance at high temperatures remains a challenge due to the structural deterioration of the electrode and electrolytes caused by the ultrafast transfer of ions.[53–54] A few studies have been conducted on SIBs, including the high-temperature range (> 50 °C), which reveals low charge/discharge efficiency and poor cycling performance.[7,55–56] The large radius of Na^+ (1.02 Å) slows the reaction kinetics and generates serious volume expansion, which hinders their practical application. Thus, it is imperative to develop superior high-temperature electrode material for SIB.

Herein, we report microwave-assisted synthesis and characterization of a 2D crystalline triazine-based polyimide **COF** and three different nanocomposite materials **COF@CNT-X** (where X = 10, 30, and 50 wt% of NH_2-MWCNT). These materials have been tested as cathodes for SIB, and **COF@CNT-50** displayed the highest specific capacity (164.3 mAh g^{-1} at 25 mA g^{-1}) and long-term cyclic performance at high current density (1000 cycles at 0.5 A g^{-1}). Additionally, we have tested **COF@CNT-50** nanocomposite for Na^+ ion storage at elevated temperature (65 °C), which exhibited considerable specific capacity with stable cycling performance. Such studies in COF and related composite materials are yet to be reported. Lastly, density functional theory (DFT) calculations were carried out to explain the atomistic origins of the experimentally observed capacity, voltages, Na^+ binding sites, and **COF**'s energy per unit cell.

2. Results and Discussion

The pristine **COF** was synthesized from the polyimide condensation of triazine triamine [TAPTz] (Scheme S1, Figure S1–S2) and pyromellitic dianhydride [PMDA] monomers in m-cresol/isoquinoline solvent mixture by microwave-assisted solvothermal technique at 160 °C in 10 min by following the earlier report from our group (Scheme 1, S2).[57] Microwave-assisted synthesis is well-known for transferring heat faster and more homogeneous than conventional solvothermal heating.[58] Thus, we could synthesize the **COF** in a microwave reactor 720 times faster than in the previously reported solvothermal methods.[44,59–60] To assess the crystallinity of the **COF**, powder X-ray diffraction (PXRD) measurement with Cu K_α radiation (λ = 1.5406 Å) was performed. Next, PXRD patterns for AA (eclipsed) and AB (staggered) stacking models were simulated, and the experimental pattern agreed with the simulated AA pattern for **COF**. The final unit cell parameters ($a = b = 36.823$ Å, $c = 3.565$ Å; $\alpha = \beta = 90°$, $\gamma = 120°$) and P_6/mmm space group were yielded after Pawley refinement on experimental PXRD pattern, which showed small differences and low residual values ($R_{wp} = 3.92\%$ and $R_p = 3.14\%$) (Figure 1a, S3, Table S1–S2). Fourier-transform infrared spectroscopic (FTIR) studies were carried out to identify the polyimide network of **COF** (Figure 1b, S4). As can be seen, three characteristic peaks at 1355, 1723, and 1778 cm^{-1} were observed for **COF** due to the symmetric vibration of formed −C−N−C- moiety and symmetric/asymmetric vibrations of carbonyl (−C=O) groups of the pyromellitic imide rings, respectively.[44,59–60] The disappearance of −N−H stretching bands at 3324 and 3210 cm^{-1} from the TAPTz building block further corroborated the successful formation of the polyimide framework in **COF**. The solid-state ^{13}C nuclear magnetic resonance (^{13}C NMR) spectrum of **COF** displayed a peak at 164 ppm for the carbonyl carbon of the imide ring. Additionally, it showed other aromatic carbon peaks between the chemical shifts of 110–140 ppm (Figure 1c). By using the same procedure, nanocomposite materials were prepared by adding 10, 30, and 50 wt% of amino-functionalized multiwalled carbon nanotube (NH_2-MWCNT) through the *in situ* polymerization of COF on the surface of NH_2-MWCNT. The composite materials is denoted as **COF@CNT-X**, where X = 10, 30 and 50 wt% of NH_2-MWCNT (Scheme S3). The PXRD patterns of the **COF@CNT-X** composites showed an additional, prominent diffraction at 26.3° for amino-functionalized MWCNT along with the diffractions of the COF (Figure 1d). The broad peak at 26.3° attributed to (002) reflections of the hexagonal graphite structure in the MWCNT layers.[61–62] The **COF@CNT-X** composites were further characterized by the FTIR study, which displayed similar characteristic vibrational peaks to **COF** (Figure 1b, S4). To comprehend the covalent linking between **COF** and NH_2-MWCNT, a model compound, namely, PMDA-CNT was also synthesized by following a similar microwave pathway by taking PMDA monomer and NH_2-MWCNT (Supporting Information). Notably,

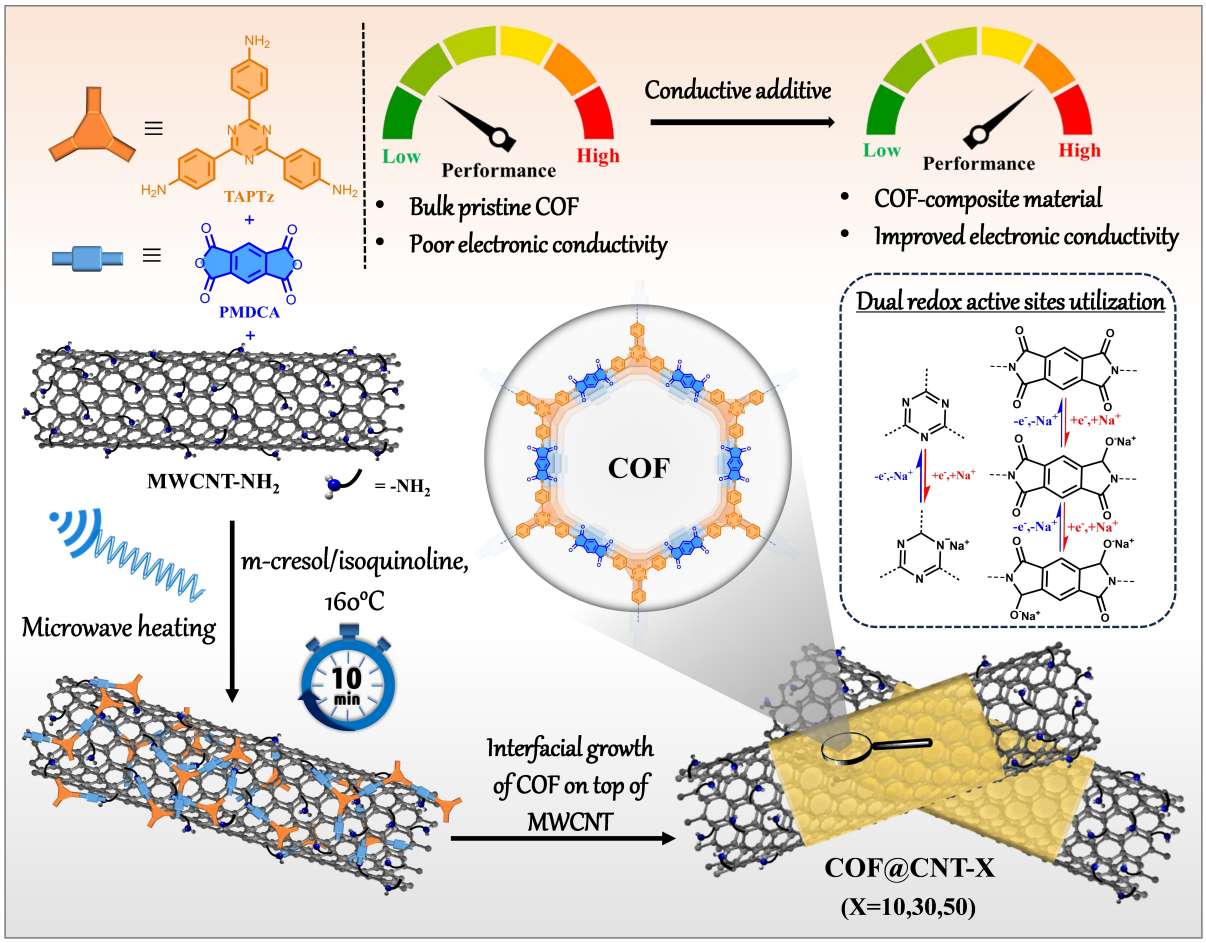

Scheme 1. Schematic representation of microwave-assisted **COF@CNT-X** nanocomposite synthesis. Here, amino-functionalized MWCNT (MWCNT-NH_2) acts as a template for the interfacial growth of **COF** on top of the MWCNTs via covalent linking. In the **COF@CNT-X**, electrochemical performance increases compared to **COF** due to higher redox active sites utilization during the Na^+ insertion/extraction process.

the FT-IR spectrum of PMDA-CNT showed a new peak for −C=O (1681 cm^{-1} and 1746 cm^{-1}) and −C–N–C− (1351 cm^{-1}) bonds, as well as a decrease in the intensity of NH_2 stretching bands (3100–3300 cm^{-1}) compared to NH_2-MWCNT (Figure S5). These results certify the covalent connection between the amine and anhydride groups from NH_2-MWCNT and PMDA, respectively.

The porosity of **COF** and **COF@CNT-X** nanocomposites was evaluated by N_2 sorption experiments at 77 K (Figure 1e). A reversible type-IV isotherm was observed for **COF** and BET surface area was calculated to be 1256.2 $m^2 g^{-1}$. With the increased wt% of NH_2-MWCNT, the BET surface area of **COF@CNT-X** composites decreased gradually from 731.1 $m^2 g^{-1}$, 523.6 $m^2 g^{-1}$ to 395.7 $m^2 g^{-1}$, respectively. The pore size distribution profile obtained by nonlocal density functional theory (NLDFT) revealed a dominant pore at around 2.3 nm for **COF**. In the case of **COF@CNT-X** also dominant pores around 2.3 nm along with other mesopores in the range of 4–8 nm were observed (Figure S6). High thermal stability up to 500 °C under the N_2 atmosphere was observed from the thermogravimetric analysis (TGA) of **COF**. Further, **COF@CNT-X** composites showed a slightly higher degradation temperature than COF, manifesting increased thermal stability and mechanical strength after covalent integration of CNT into the framework (Figure S7). The **COF** showed chemical stability in different solvents, making it advantageous for preparing electrodes in battery applications. After soaking in water and common organic solvents for 48 h, the PXRD pattern of **COF** was recorded, indicating stability of the framework (Figure S8). The morphology of the **COF** and **COF@CNT-X** composites was examined using field emission scanning electron microscopy (FESEM) and transmission electron microscopy (TEM) (Figure 1f, S9). FESEM images of pristine **COF** displayed fibrous morphology consisting of agglomeration of small nanosheets (Figure S9), while **COF@CNT-X** composites consist of smooth tubular surfaces (Figure 1g, S9). Further, TEM and high-resolution TEM (HRTEM) probed the successful wrapping of the **COF** layers on top of the MWCNT, forming tube-type core-shell structures (Figure 1h–1i, Figure S9). Further, atomic force microscopy (AFM) measurement was carried out, which demonstrated the fibrous morphology of the pristine **COF** with a height of 35 ± 2 nm and a width of 380 ± 20 nm (Figure S10). The AFM image of entangled CNT shows a height of 15 ± 2 nm and a width of 80 ± 10 nm (Figure S10). The AFM imaging and corresponding height profile analysis (Figure S10) also show a similar fibrous morphology for **COF@CNT-X**, but

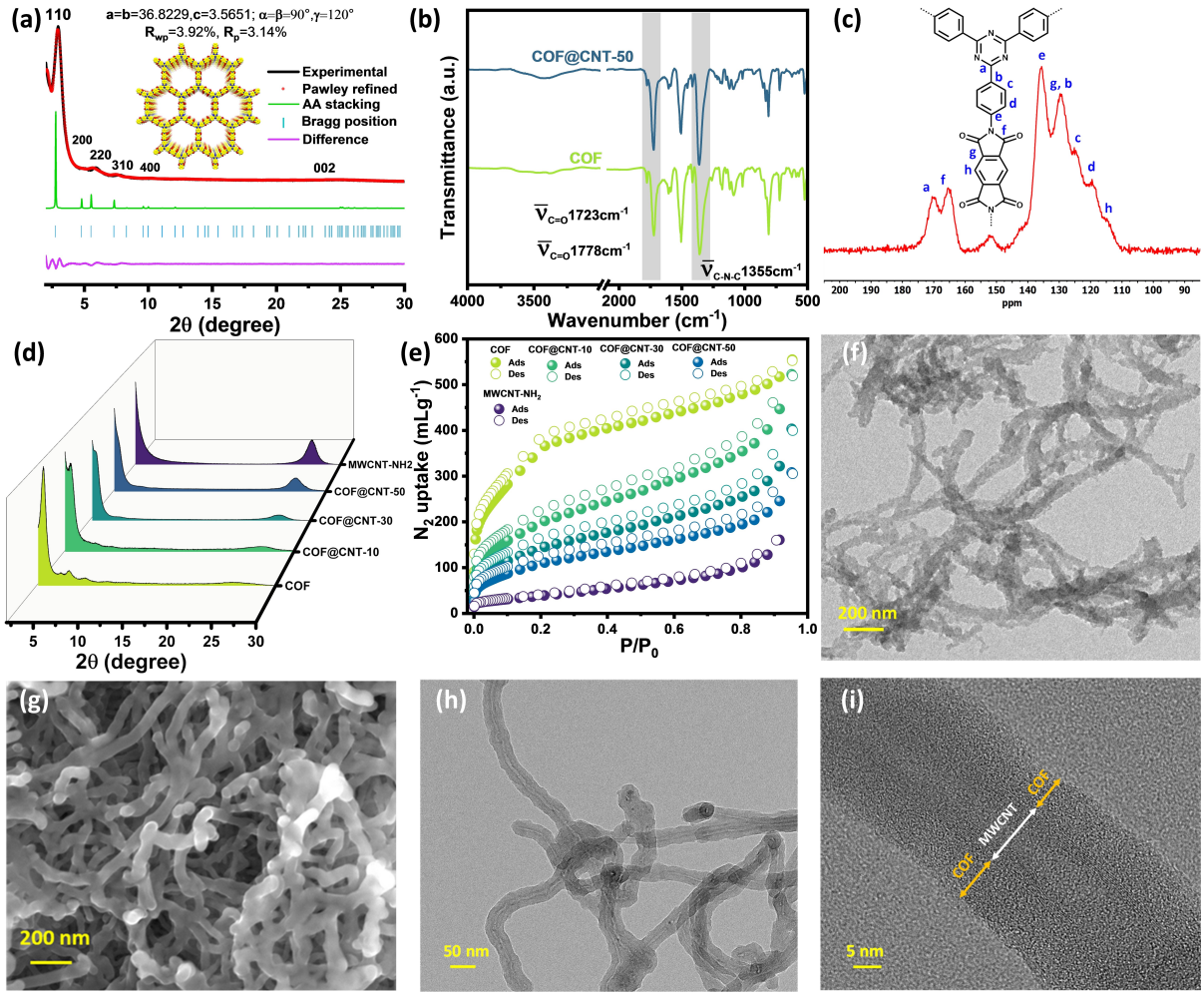

Figure 1. (a) PXRD patterns of **COF**; experimentally obtained (black), Pawley refined (dotted red), their difference (purple), simulated pattern for AA stacking (green) and Bragg positions (sky blue). (b) FT-IR spectra of **COF** and **COF@CNT-50** nanocomposite. (c) Solid-state ^{13}C NMR spectrum of **COF**. (d) PXRD patterns of **COF@CNT-X** composites (where X = 10, 30 and 50 wt% of NH_2-MWCNT), along with **COF** and MWCNT-NH_2. (e) N_2 sorption isotherm at 77 K for **COF**, all three **COF@CNT-X** composites, and MWCNT-NH_2. (f) TEM image of **COF**. (g) FESEM image of **COF@CNT-50** composite. (h) TEM image of **COF@CNT-50** composite. (i) High-resolution TEM image of **COF@CNT-50** clearly demonstrates the interfacial growth of **COF** layers on top of CNTs.

with larger dimensions: a height of 80 ± 5 nm and a width of 500 ± 20 nm. The increased composite dimensions compared to pristine **COF** and CNT indicate uniform growth of **COF** layers around the CNT. Thus, it can be stated that covalent linking between the -NH_2 group of MWCNT and residual anhydride moieties of **COF**, as well as strong π–π interaction, drives the interfacial growth of **COF** on MWCNT. This process eventually forms tube-type core-shell structures. Moreover, energy dispersive X-ray mapping analysis of **COF@CNT-50** showed a uniform distribution of carbon, nitrogen, and oxygen elements (Figure S11).

The electrochemical performance of **COF** and **COF@CNT-X** composites was conducted in a CR2032-type coin half-cell within the potential window of 1.3–3.5 V. Coin cells were assembled with **COF** or **COF@CNT-X** composites as the positive electrode, Na foil as the counter electrode and 1 M $NaPF_6$ in diglyme was used as the electrolyte. Cyclic voltammetry (CV) of **COF** and **COF@CNT-X** composites at a scan rate of 0.3 mV s^{-1} demonstrated two prominent reversible redox peaks at 1.58/1.70 V and 2.12/2.19 V (*vs.* Na^+/Na) indicating the reversible sodiation (reduction)/desodiation (oxidation) processes (Figure 2a, S12). Even though **COF**'s structural units provide dual active sites for the charging and discharging processes: i) −C=O groups (from the PMDA motif) and ii) −C=N− groups (from the TAPTz motif), we only observed two reversible peaks in CV primarily associated with the two-step, two-electron reaction of the −C=O groups. This infers that the redox peaks from the −C=N− groups were less prominent and overlapped with those from the −C=O group. The reason for this phenomenon is that the −C=N− groups are less exposed towards sodiation/desodiation processes as they are located in the centre of the TAPTz building block. Interestingly, it was also observed that the CV areas and peak current densities were increased as the mass content of CNT increased in the **COF@CNT-X** composites (Figure S12). This fact can be attributed to the interfacial growth of a few layers of **COF** on top of the intrinsically conductive CNTs, which shortens the Na^+ ion diffusion length and improves the Na^+ storage characteristics across the bulk

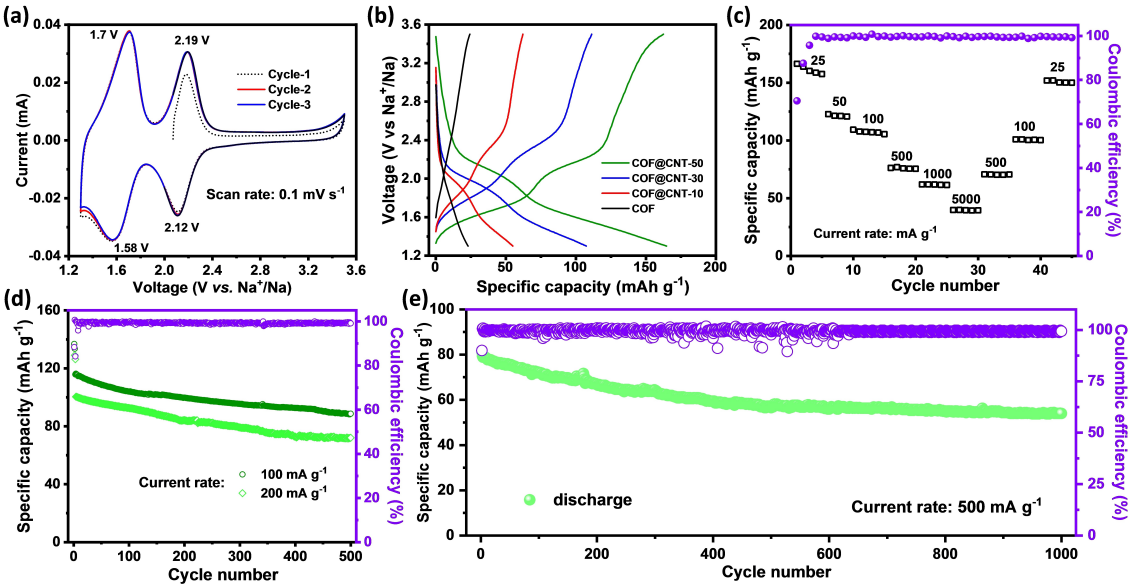

Figure 2. (a) CV profiles of **COF** at a scan rate of 0.1 mV s^{-1}; (b) Galvanostatic charge/discharge profiles at 25 mA g^{-1} for **COF** (black), **COF@CNT-10** (red), **COF@CNT-30** (blue) and **COF@CNT-50** (green). (c) Rate performances of **COF@CNT-50** at 25–500 mA g^{-1} current densities. (d) Cycling performances over 500 cycles with coulombic efficiency at 100 mA g^{-1} and 200 mA g^{-1} for **COF@CNT-50** composite. (e) Long-term cycling performance of **COF@CNT-50** composite at 500 mA g^{-1} up to 1000 cycles.

electrode. **COF@CNT-50** exhibited the highest CV area, indicating the most effective utilization of redox-active sites among all four active cathode materials. Next, galvanostatic charge/discharge (GCD) experiments were conducted in the voltage window of 1.3 to 3.5 V for all four composites of the positive electrodes (Figure 2b) at 25 mA g^{-1} current rate at the same voltage window. The pristine **COF** showed a reversible capacity of ~18.5 mAh g^{-1} after 30 cycles, whereas the **COF@CNT-50** showed ~138.5 mAh g^{-1} (Figure S13a), which indicates as the percentage of CNT increases, the reversible capacity also increases. The first cycle GCD profile for **COF@CNT-50** is shown in Figure S13b, demonstrating an initial coulombic efficiency of approximately 95.6%, which retains the two pairs of peaks observed in the CV very well. The 2nd cycle galvanostatic charge-discharge profile at 25 mAg^{-1} reveals that **COF** has a specific capacity of 23 mAh g^{-1}, much less (~14%) compared to its theoretical capacity (calculation in Supporting Information, Figure S14) arises due to low utilization of active sites of the 2D stacked multilayer framework. However, the specific capacity at 25 mA g^{-1} in **COF@CNT-10**, **COF@CNT-30**, and **COF@CNT-50** increased to 55.2, 108.1, and 164.3 mAh g^{-1}, respectively, based on the total active mass of the material (mass of **COF**, MWCNT-NH_2, and carbon black). In the **COF** unit cell, the maximum available Na^+ binding site is 12 (6 pyromellitic 'O' and 6 triazine 'N'), and the corresponding theoretical capacity is 255.2 mAh g^{-1}. This capacity is much higher than the experimentally observed capacity of **COF@CNT-10** composites. This indicates that all the available redox sites in **COF** are not participating in the charge/discharge process. Considering that there are 8 Na^+ ions involved in each **COF** unit cell, the utilization of redox-active sites was determined to be 33, 64, and 97% for **COF@CNT-10**, **COF@CNT-30**, and **COF@CNT-50**, respectively (calculated theoretical specific capacity = 170.1 mAh g^{-1}) (Figure S14, Table S3). Furthermore, the specific capacity of the monomer building units (i.e., PMDA, TAPTz) and MWCNT-NH_2 was also measured at 25 mA g^{-1} (Figure S15). The low specific capacity of MWCNT-NH_2 illustrates that **COF** contributes significantly to achieving high reversible capacity in the **COF@CNT-X** composites after high utilization of the active sites. Compared to the PMDA and TAPTz monomers, **COF** and **COF@CNT-X** composites exhibited significantly higher and more stable performance. This highlights the polymeric electrodes' good stability in the electrolytic solution.

Further, we conducted more in-depth electrochemical studies with **COF@CNT-50** composite only as it shows the best performance among all **COF@CNT-X** composites and **COF**. The rate capability across various current densities is a crucial parameter for electrode materials. To assess high-current rate capability, the SIB cell with **COF@CNT-50** underwent testing across a range of 25–5000 mA g^{-1} current densities (Figure 2c). Initially, the cell demonstrated a reversible capacity of approximately ~157 mAh g^{-1} at a current rate of 25 mA g^{-1}. Subsequently, as current densities increased to 50, 100, 500, and 1000 mA g^{-1}, reversible capacities decreased to approximately ~121, 105.8, 75.2, and 61.5 mAh g^{-1}, respectively. This represents a restoration of approximately ~77%, 67.3%, 47.9%, and 39.1% of reversible capacity when current densities increased by two, four, twenty, and forty times, respectively, compared to the initial current density. Moreover, the SIB cell was subjected to a very high current density of 5000 mA g^{-1} yet maintained a reversible capacity of around ~39.3 mAh g^{-1}. Upon reverting to its initial current density in three steps, the electrode exhibited a reversible capacity of approximately 150 mAh g^{-1} with stable cycling, representing a restoration of approximately 95.5%

capacity. The SIB cell maintained a coulombic efficiency of approximately 100% throughout the rate performance, confirming the excellent rate capability of the **COF@CNT-50** electrodes, as demonstrated by these results. Long-term cycling stability is also an essential parameter in estimating cell performance. The long-term cycling experiment of **COF@CNT-50** was initially studied through 500 cycles of repeated charge/discharge operations at current densities of 100 and 200 mA g^{-1}. It exhibits outstanding cycling performance, retaining 78% and 74% of its initial capacity after 500 cycles at 100 and 200 mA g^{-1}, respectively, with a coulombic efficiency of ~100% (Figure 3d). Further, we have conducted cycling experiments up to 1000 cycles at a higher current rate of 500 mA g^{-1}. After 1000 cycles, ~69% of capacity retention with ~100% coulombic efficiency was observed, which indicates stable active site utilization of **COF@CNT-50** for a longer time (Figure 3e). Additionally, no change was observed in the FT-IR spectrum and HRTEM image of the **COF@CNT-50** after 1000 times GCD cycles (Figure S16–S17), suggesting good structural stability of the electrode material. In Table S4, the electrochemical performance of **COF@CNT-50** as an organic cathode material for SIB was further compared with the earlier reported organic polymer-based positive electrodes for SIB.

2.1. High-Temperature SIB Application

The elevated temperature battery operation is important for next-generation energy storage applications.[55] To check the high-temperature performance of the **COF@CNT-50** composite as a sodium-ion battery (SIB) cathode, we conducted tests on the cell at an elevated temperature of 65 °C. The SIB cell was tested at 65 °C within a voltage window of 1.3–3.5 V and a current rate of 300 mA g^{-1} (Figures 3a and 3b). Figure 3a illustrates the galvanostatic charge-discharge (GCD) profiles across different cycles, from the 2nd to the 300th cycle, exhibiting a similar pattern to that observed at room temperature (Figure 2b). The initial reversible capacity of the first cycle was approximately 83.5 mAh g^{-1} at a current density of 300 mA g^{-1} (Figure 3b). However, after a few cycles, a slight capacity fade was observed, resulting in a reversible capacity of around 63.3 mAh g^{-1} after 300 cycles, representing approximately ~76% capacity restoration. The coulombic efficiency remained at approximately ~95.3% after 300 cycles, indicating the excellent cycling stability of the **COF@CNT-50** electrode under high-temperature conditions. Upon continuous cycling, the plateaus of GCD profiles are somehow missing; there could be several reasons behind it (Figure 3a). Prolonged cycling at high temperatures can induce irreversible changes at the electrode/electrolyte interface, such as SEI layer thickening or instability, which impair sodium-ion kinetics and diminish the definition of voltage plateaus. While the initial cycles may display activation behavior with well-defined plateaus, continuous cycling can lead to the passivation of active sites due to surface reactions, producing a sloping voltage profile. Additionally, sodium-ion diffusion at high temperatures may create uneven distribution within the material, contributing to a gradient that smoothens the plateaus.

However, slight fluctuations in capacity and variations in coulombic efficiency (CE) under high-temperature conditions were observed, which can be attributed to several factors. Elevated temperatures may induce reversible and irreversible structural changes in COF materials, potentially altering ion transport pathways or causing partial degradation, leading to capacity variations during cycling. Moreover, non-uniform plating and stripping of sodium on electrode surfaces at high temperatures can result in intermittent capacity changes. To the best of our knowledge, this level of high-temperature SIB performance has not been reported previously. This study underscores the superiority of COF-based materials for next-generation SIB applications in both room and high temperatures.

To understand the charge storage process, the electrochemical reaction kinetics of **COF@CNT-50** was investigated by CV measurement at various scan rates (ν) from 0.1 to 1.0 mV s^{-1} (Figure 4a). Two pairs of redox peaks (A_1, A_2, O_1, and O_2) are slightly shifted as the scan rate increases, demonstrating the favourable redox capacity of **COF@CNT-50** even at high current

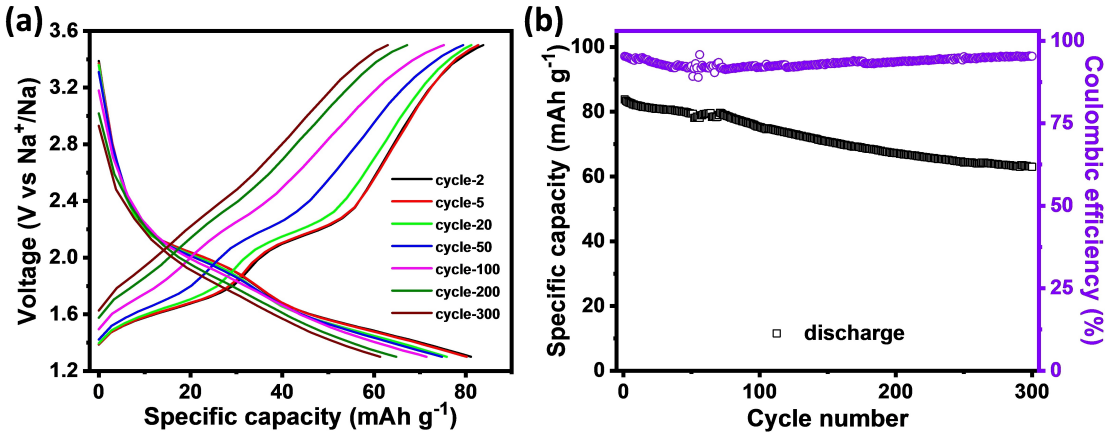

Figure 3. (a) At high temperature (65 °C), charge/discharge profile of **COF@CNT-50** composite after different cycle numbers at 300 mA g^{-1}. (b) Cycling performances over 300 cycles with coulombic efficiency at 100 mA g^{-1} for **COF@CNT-50** composite.

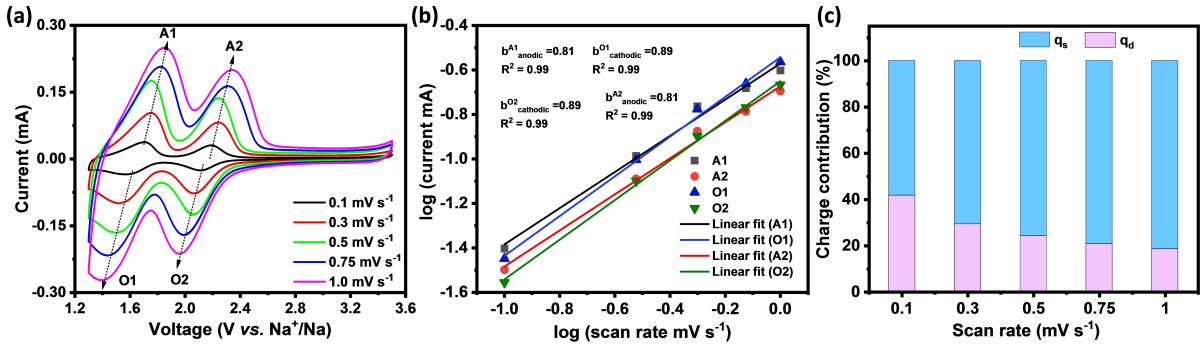

Figure 4. (a) CV measurements of **COF@CNT-50** recorded under different scan rates (0.1–1.0 mV s^{-1}) to understand the electrochemical reaction kinetics of charge storage process. (b) Plot of log i vs log ν to evaluate the *b* values of different peaks. (c) Contribution of pseudocapacitive and diffusion currents at different scan rate.

densities. Further, the peak current (i) and scan rate (ν) are fitted by the equation of log i = *b* log ν + log *a*; where the *b* value reflects capacity storage behaviours. A redox reaction controlled by a semi-infinite linear diffusion process gives *b* value of near 0.5, while for a surface-controlled pseudocapacitive process, the *b* value is near 1.[63–65] The *b* values of four redox peaks A_1, A_2, O_1, and O_2 are found to be 0.81, 0.81, 0.89 and 0.89 (Figure 4b). This indicates the surface-controlled pseudocapacitive storage process in **COF@CNT-50** due to the high utilization of the **COF**'s redox-active pyromellitic and triazine groups. In addition, the contribution of pseudocapacitance to the overall capacity storage is computed using the equation $i = k_1\nu + k_2\nu^{1/2}$, whereas k_1 and k_2 are constants and $k_1\nu$ and $k_2\nu^{1/2}$ reflect the contribution from pseudocapacitance and ion diffusion capacitance, respectively.[63–65] k_1 and k_2 constants can be deducted by plotting $i\nu^{-1/2}$ vs $\nu^{1/2}$. At the low scan rate of 0.1 mV s^{-1}, the capacitive contribution is 58%, which is increased to 82% at 1 mV s^{-1}. These results further suggest that Na^+ storage in **COF@CNT-50** is a kinetically fast pseudocapacitive process (Figure 4c).

The progress of the redox reaction during Na^+ insertion/extraction was monitored using *ex situ* XPS measurement, and the results were referenced to the C1s peak (284.4 eV) (Figure 5). After sodiation (discharge) process, C1s spectrum of pristine **COF@CNT-50** was deconvoluted into −C=C− (284.7 eV), −C−C−/−C=N−/ −C−N− (285.2 eV), −C−O− (286.4 eV) and −C=O (287.9 eV), respectively (Figure 5a).[12,45,66] The peaks appeared at 286.4 eV (−C−O−) and 287.9 eV (−C=O) representing the insertion of Na^+ into the pyromellitic group of the material (Figure 5a). The involvement of −C=N− moieties from the triazine building block was also observed from deconvoluted N1s XPS spectra (Figure 5b). A low-intensity peak for −C−N− bonds (399.6 eV) emerged after the sodiation process, indicating the poor Na^+ storage at the −C=N− sites of the **COF**. Once the charging procedure is completed, the following peak becomes even weaker (Figure 5b).[15,50,67] The deconvoluted O1s XPS spectra demonstrated that the intensity of O−C− groups (529.8 eV) is increased compared to O=C− groups (531.2 eV) after the sodiation. This further indicating the Na^+ insertion process into −C=O groups to form −C−O$^-$$Na^+$

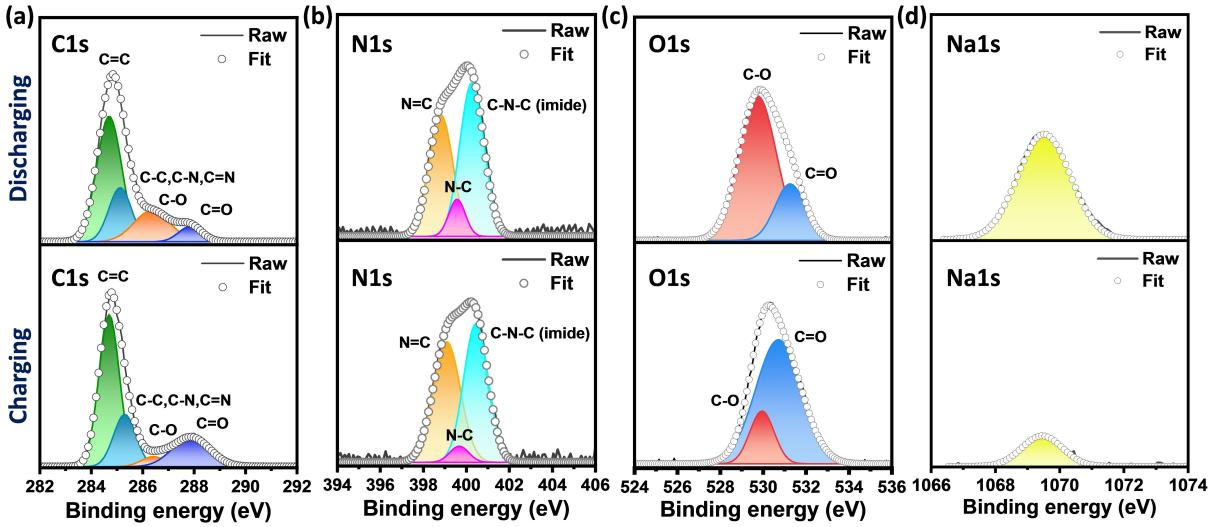

Figure 5. Deconvoluted XPS spectra of (a) C1s (b) N1s and (c) O1s after discharging and charging process of **COF@CNT-50** electrode. (d) Na^+ insertion and extraction mechanism occurring in the redox-active pyromellitic carbonyl (−C=O) and triazine (−C=N−) group during the charging and discharging processes.

(Figure 5c). During the desodiation process, the intensity of −C–O$^-$Na$^+$ groups decreased along with the simultaneous increase of −C=O groups (Figure 5c), evincing reversible Na$^+$ combined with electroactive −C=O groups in **COF@CNT-50**.[44,68] Further, the reduced Na 2p peak (1069.5 eV) intensities in desodiation process suggesting the involvement of reversible Na$^+$ insertion/extraction process. (Figure 5d).[65]

To understand the arrangement of the 8 Na$^+$ per unit cell of the **COF** (based on the maximum observed specific capacity of **COF@CNT-50**), we performed DFT calculations with the Vienna Ab-initio Simulation Package (VASP),[69–70] using the strongly constrained and appropriately normed (SCAN)[71] meta-generalized gradient approximation exchange-correlation functional (description of calculation parameters given in the Supporting Information). For all calculations, we considered the crystalline unit cell of **COF**, where a total of 18 sites are available for binding Na$^+$ ions (Figure S18). Among the 18 sites, we considered a maximum occupation of 12 sites, resulting in a maximum Na content of x = 12 in Na$_x$**COF**. From here on, 'x' in Na$_x$**COF** denotes the COF's number of Na per unit cell (or per ring). Thus, the stability of any Na-containing **COF** structure is evaluated using the empty **COF** (i.e., Na$_0$**COF**) and the fully sodiated **COF** (i.e., Na$_{12}$**COF**) as the reference states (Figure 6a). Instead of the previously used molecular electrostatic potential (MESP) method[45,72] where multiple Na$^+$ are placed at every electrostatic potential global minimum around a **COF**, we adopted a thermodynamics-based, sequential Na$^+$ addition approach (Supporting Information) to determine all the stable sodiated-**COF** configurations. During sodiation, multiple Na$^+$ may not always bind a **COF** unit simultaneously since each Na$^+$ binding to the **COF** can cause significant structural and electronic changes. These effects can impact the energetics of further sodiation process in the unit cell of **COF**. The changes caused by the binding of each Na$^+$ are impossible to predict if multiple Na$^+$ are attached to the **COF** simultaneously. Our sequential Na$^+$ addition approach thus enables us to observe the changes in the **COF** with every incremental Na$^+$ addition to the unit cell, yielding unique insights and accurate predictions that match closely with experiments.

The first Na$^+$ entering the **COF** unit cell binds to the triazine −C=N− instead of the pyromellitic −C=O redox-active site (Figure S19a), with the Na–N binding energy ~2 eV atom^{-1} lower than the Na–O case. While Na$^+$ binding to N (single lone pair of electrons) instead of O (two lone pairs of electrons) is

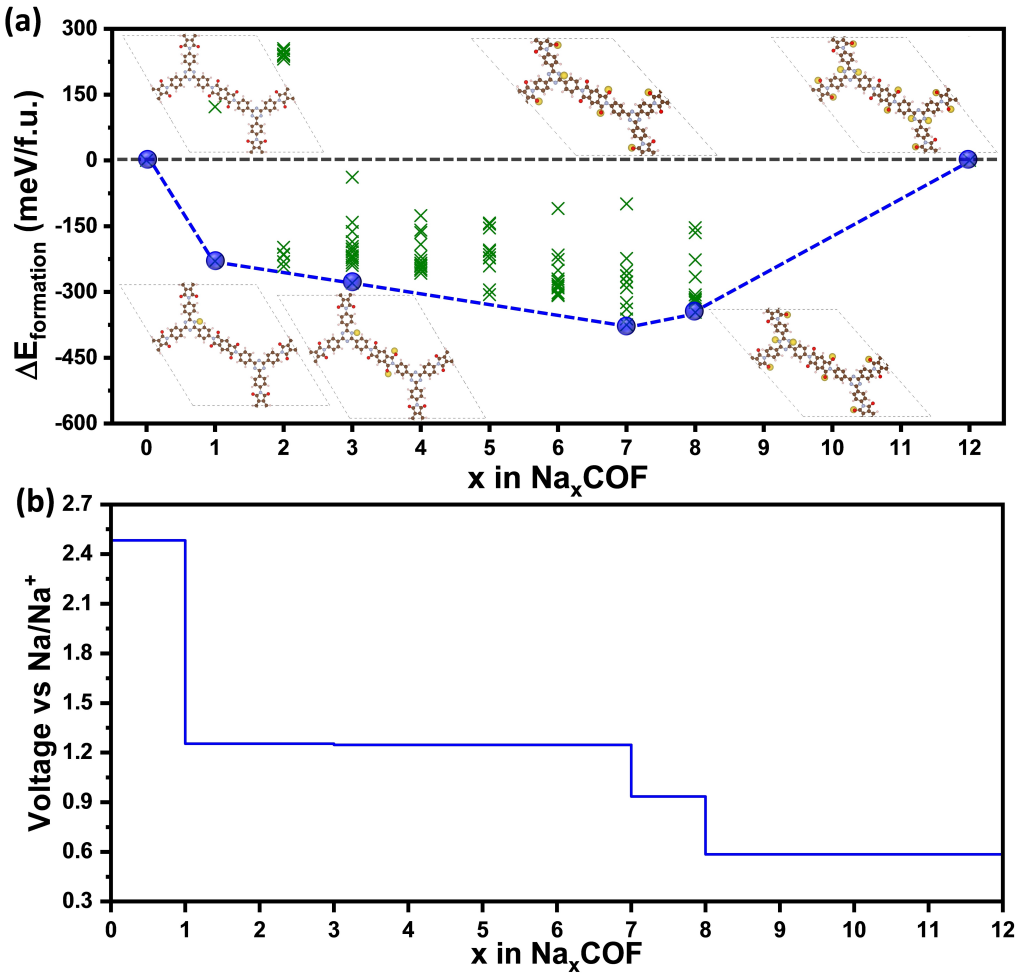

Figure 6. (a) DFT calculated pseudo-binary convex hull, which shows the stable (blue dots) and metastable/unstable (green crosses) configurations of Na$_x$**COF**, where x ranges from 0 to 12. (b) DFT calculated the average Na intercalation voltage versus Na-content within the COF structure.

unexpected, we observe that Na^+ binding to the triazine −C=N− breaks the planarity of the **COF** (Figure S19b). In this non-planar structure, the Na^+ simultaneously binds to two triazine N atoms in adjacent A–A stacked layers. On the other hand, the **COF** remains planar when a single Na^+ binds to the pyromellitic O (i.e., Na^+ binds to a single pyromellitic O on the same plane, Figure S19c,d). Thus, the breaking of the symmetric **COF** structure to form non-planar Na–N bonds enables the Na^+ to preferably bind at the triazine −C=N− site over the pyromellitic −C=O site. Upon further sodiation of the non-planar Na_1**COF** structure, Na^+ prefers binding to the pyromellitic O sites until seven Na-ions are in a unit cell (i.e., until Na_7**COF**, see Figure S21–S23). Also, we observe an increase in the shearing of the **COF** rings with increasing Na^+ in the structure (Figure S24). With seven Na^+ per unit cell, each pyromellitic unit accommodates two Na^+ (Figure S20), with non-identical arrangement of Na^+ among the pyromellitic units. For example, in a planar **COF**, two Na^+ can bind to diagonal O sites in a pyromellitic unit to minimize electrostatic repulsion (Figure S20a). However, in the non-planar **COF** that we obtain beyond Na_1**COF**, we observe some pyromellitic units where two Na^+ bind to adjacent O sites (Figure S20b) and other pyromellitic units with a distorted diagonal arrangement of two Na^+ (Figure S20c). The pyromellitic units with Na^+ bound to adjacent O sites are the closest to the first Na^+ bound to a triazine unit. This indicates some electronic rearrangement among the π-bonds that enables Na^+ to bind to adjacent O sites. The pyromellitic units that are further from the first bound Na^+ site facilitate Na^+ binding at the distorted diagonal sites. With every pyromellitic unit populated with two Na^+ in Na_7**COF**, the eighth Na^+ binds to a triazine −C=N− group. Interestingly, the final Na^+ binds to the same triazine unit as the first Na^+, leaving a completely unoccupied triazine unit in the Na_8**COF** structure (Figure S22d). The proximity of two Na^+ in a single triazine unit implies possible electronic redistribution in the **COF** structure, which dominates any steric effects and makes the occupied triazine unit more favourable for Na^+ binding.

To understand the thermodynamic stability (at 0 K) of different Na-containing **COF** configurations and their Na-intercalation behavior, we obtained the pseudo-binary convex hull (Figure 6a). We also calculated the average Na intercalation voltage versus Na-content plots (Figure 6b). The convex hull showed that Na_1**COF**, Na_3**COF**, Na_7**COF**, and Na_8**COF** are the only stable sodiated **COF** phases. As shown in Figure 6a, the reference phases Na_0**COF** and Na_{12}**COF** are depicted using blue dots and dashed blue lines while other metastable configurations are marked with green crosses. Thus, we expect phase-separating behaviour at compositions between the stable compositions. For example, at Na_2**COF**, we expect the **COF** structure to form Na-poor (Na_1**COF**) and Na-rich (Na_3**COF**) domains. Figure 6b references the average Na intercalation voltage concerning the Na/Na^+ electrode. Combining the six stable phases in the convex hull, including the reference configurations (Figure 6a), leads to five voltage plateaus in the voltage-composition curve. Each voltage plateau represents a range of Na-contents of constant Na^+ chemical potential, resulting from two-phase equilibria among the stable sodiated-**COF** phases. On the other hand, voltage steps represent varying Na^+ chemical potential or a single phase region (i.e., a single stable compound) in the convex hull. Thus, the first voltage plateau at ~2.5 V is due to the coexistence of Na_0**COF** and Na_1**COF** phases, which is followed by a voltage step from ~2.5 V to ~1.25 V corresponding to the stable Na_1**COF**. Similarly, the voltage plateaus at ~1.25 V, ~1.24 V, ~0.93 V and ~0.59 V are due to Na_1**COF**−Na_3**COF**, Na_3**COF**−Na_7**COF**, Na_7**COF**−Na_8**COF** and Na_8**COF**−Na_{12}**COF** coexistence, respectively and every step between these plateaus correspond to single phases Na_3**COF**, Na_7**COF** and Na_8**COF**, respectively. Note that ground states that are "shallow", i.e., states that cause a minimal change in slope of the convex hull concerning its adjacent stable phases, cause a minor voltage step. This is why we observe a negligible voltage step (~0.01 V) during the formation of Na_3**COF**. The transition of Na_8**COF** to Na_x**COF** ($x > 8$) upon sodiation reduces the voltage below 0.93 V vs. Na/Na^+ (Figure 6b). At such low voltages, the Na^+ chemical potential difference between the cathode and the anode is small, leading to an insignificant driving force for Na^+ intercalation into the cathode, potentially making it difficult to practically sodiate the **COF** beyond $x = 8$. Thus, eight Na^+ per unit cell of **COF** likely mark a practical limit to its capacity, in agreement with our experimentally observed capacity. This is one of the reasons that we did not sequentially add Na^+ for $x = 9$, 10, and 11 in Na_x**COF**. Overall, our calculated voltage profile, from Na_0**COF** to Na_8**COF**, is qualitatively consistent with the voltage profiles obtained experimentally. For example, the experimental voltage plateaus at ~2.2 V and ~1.2 V, visible especially during charging (Figure 2b) of **COF@CNT-50**, are in close agreement with the theoretical voltage plateaus at ~2.5 V and ~1.25 V. The gentle slopes in the experimental voltage plateaus are usual since the measured voltages are at ambient temperatures and not at 0 K. The initial high voltages in the experimental voltage-capacity curves are likely due to capacitive currents in galvanostatic measurements and cannot be captured within the thermodynamic treatment of DFT.

3. Conclusions

In summary, we synthesized **COF@CNT-X** (X = 10, 30, 50) nanocomposite materials for SIB cathodes, combining a stable polyimide-based **COF** with amino-functionalized multiwalled carbon nanotubes (MWCNT-NH_2) within 10 minutes using microwave assistance. High-resolution TEM confirmed the formation of tube-type core-shell structures with thin **COF** layers grown covalently on MWCNTs' outer surface. This synergy enhanced mechanical stability, electrical conductivity, and redox-active site accessibility in **COF@CNT-X** nanocomposites. **COF@CNT-50** showed a high capacity of 164.3 mAh g^{-1} at 25 mA g^{-1}, with 69% capacity retention after 1000 cycles at 500 mA g^{-1}. At 65 °C, stable electrochemical performance was maintained with ~76% capacity restoration after 300 cycles and ~95.3% coulombic efficiency. *Ex situ* XPS measurements and theoretical calculations revealed the charge storage mechanism based on reversible Na^+ insertion/extraction with −C=O and

−C=N− groups in **COF@CNT-50**. Further, we explained the COF's experimentally observed voltage and capacity at the atomic level by performing DFT-based calculations, which revealed the structural evolution and the startling arrangement of Na-ions in the COF ring during sodiation. This study highlights the utilization of dual active sites for high-performance cathode material and promotes further research and development of cutting-edge COF materials for SIBs at both ambient and elevated temperatures.

Acknowledgments

A.D. acknowledge the CSIR (Government of India) for a fellowship. S.B. thank the Science and Engineering Research Board (SERB), Department of Science and Technology (DST) for National Postdoctoral fellowship (NPDF). T.K.M. acknowledges the SERB, Department of Science and Technology (Projects SPR/2021/000592), RAK-CAM (from UAE), SSL, ICMS, and JNCASR for financial support. The SAMat research facility and Sheikh Saqr senior fellowship are also gratefully acknowledged by T.K.M. Next, A.P. thanks Lithiem OTT-SRA-24-0657 for funding. G.S.G. and S.P. gratefully acknowledge financial support from the Indian Institute of Science (IISc) and the computing time provided to them on the high-performance computer noctua1 and noctua2 at the NHR Center PC2. These computational resources was funded by the Federal Ministry of Education and Research and the state governments participating on the basis of the resolutions of the GWK for the national high-performance computing at universities (www.nhr-verein.de/unsere-partner). The computations for this research were performed using computing resources under project hpc-prf-emdft. Special thanks to Joseph Manion for helping to make the TOC image.

Conflict of Interests

The authors declare no conflict of interest.

Data Availability Statement

The data that support the findings of this study are available in the supplementary material of this article.

Keywords: COF · COF-CNT nanocomposites · Organic electrode · Sodium-ion battery · Dual active sites · High-temperature performance

[1] J. B. Goodenough, K.-S. Park, *J. Am. Chem. Soc.* **2013**, *135*, 1167.
[2] M. Fichtner, K. Edström, E. Ayerbe, M. Berecibar, A. Bhowmik, I. E. Castelli, S. Clark, R. Dominko, M. Erakca, A. A. Franco, A. Grimaud, B. Horstmann, A. Latz, H. Lorrmann, M. Meeus, R. Narayan, F. Pammer, J. Ruhland, H. Stein, T. Vegge, M. Weil, *Adv. Energy Mater.* **2022**, *12*, 2102904.
[3] J. B. Goodenough, Y. Kim, *Chem. Mater.* **2010**, *22*, 587.
[4] J. B. Goodenough, *Energy Storage Mater.* **2015**, *1*, 158.
[5] S. Wang, C. Sun, N. Wang, Q. Zhang, *J. Mater. Chem. A* **2019**, *7*, 10138.
[6] C. Vaalma, D. Buchholz, M. Weil, S. Passerini, *Nat. Rev. Mater.* **2018**, *3*, 18013.
[7] Z. Li, Y. Zhang, J. Zhang, Y. Cao, J. Chen, H. Liu, Y. Wang, *Angew. Chem. Int. Ed.* **2022**, *61*, e202116930.
[8] M. Sawicki, L. L. Shaw, *RSC Adv.* **2015**, *5*, 53129.
[9] N. Yabuuchi, K. Kubota, M. Dahbi, S. Komaba, *Chem. Rev.* **2014**, *114*, 11636.
[10] F. Kang, L. Yan, Z. Chen, Y. Zhang, Q. Gu, J. Yang, S. Xu, X. Wang, C.-S. Lee, Y. Wang, Q. Zhang, *Angew. Chem. Int. Ed.* **2024**, *n/a*, e202417779.
[11] C. Delmas, *Adv. Energy Mater.* **2018**, *8*, 1703137.
[12] M. K. Shehab, K. S. Weeraratne, T. Huang, K. U. Lao, H. M. El-Kaderi, *ACS Appl. Mater. Interfaces* **2021**, *13*, 15083.
[13] J. B. Goodenough, *J. Power Sources* **2007**, *174*, 996.
[14] C. Wang, Y. Xu, Y. Fang, M. Zhou, L. Liang, S. Singh, H. Zhao, A. Schober, Y. Lei, *J. Am. Chem. Soc.* **2015**, *137*, 3124.
[15] D.-H. Yang, Z.-Q. Yao, D. Wu, Y.-H. Zhang, Z. Zhou, X.-H. Bu, *J. Mater. Chem. A* **2016**, *4*, 18621.
[16] Y. Chen, C. Wang, *Acc. Chem. Res.* **2020**, *53*, 2636.
[17] A. Dey, F. A. Rahimi, S. Barman, A. Hazra, T. K. Maji, *J. Mater. Chem. A* **2023**, *11*, 13615.
[18] P. Poizot, J. Gaubicher, S. Renault, L. Dubois, Y. Liang, Y. Yao, *Chem. Rev.* **2020**, *120*, 6490.
[19] S. Wang, Q. Wang, P. Shao, Y. Han, X. Gao, L. Ma, S. Yuan, X. Ma, J. Zhou, X. Feng, B. Wang, *J. Am. Chem. Soc.* **2017**, *139*, 4258.
[20] A. Dey, J. Pradhan, S. Biswas, F. Ahamed Rahimi, K. Biswas, T. K. Maji, *Angew. Chem. Int. Ed.* **2024**, *63*, e202315596.
[21] J. Back, J. Park, Y. Kim, H. Kang, Y. Kim, M. J. Park, K. Kim, E. Lee, *J. Am. Chem. Soc.* **2017**, *139*, 15300.
[22] S. Gu, S. Wu, L. Cao, M. Li, N. Qin, J. Zhu, Z. Wang, Y. Li, Z. Li, J. Chen, Z. Lu, *J. Am. Chem. Soc.* **2019**, *141*, 9623.
[23] K. A. See, S. Hug, K. Schwinghammer, M. A. Lumley, Y. Zheng, J. M. Nolt, G. D. Stucky, F. Wudl, B. V. Lotsch, R. Seshadri, *Chem. Mater.* **2015**, *27*, 3821.
[24] Z. Song, Y. Qian, M. L. Gordin, D. Tang, T. Xu, M. Otani, H. Zhan, H. Zhou, D. Wang, *Angew. Chem. Int. Ed.* **2015**, *54*, 13947.
[25] J. Wu, X. Rui, C. Wang, W.-B. Pei, R. Lau, Q. Yan, Q. Zhang, *Adv. Energy Mater.* **2015**, *5*, 1402189.
[26] J. Wang, Y. Lee, K. Tee, S. N. Riduan, Y. Zhang, *Chem. Commun.* **2018**, *54*, 7681.
[27] Y.-X. Yin, S. Xin, Y.-G. Guo, L.-J. Wan, *Angew. Chem. Int. Ed.* **2013**, *52*, 13186.
[28] C. Luo, G.-L. Xu, X. Ji, S. Hou, L. Chen, F. Wang, J. Jiang, Z. Chen, Y. Ren, K. Amine, C. Wang, *Angew. Chem. Int. Ed.* **2018**, *57*, 2879.
[29] Y. Liang, Z. Chen, Y. Jing, Y. Rong, A. Facchetti, Y. Yao, *J. Am. Chem. Soc.* **2015**, *137*, 4956.
[30] S. Muench, A. Wild, C. Friebe, B. Häupler, T. Janoschka, U. S. Schubert, *Chem. Rev.* **2016**, *116*, 9438.
[31] Z. Luo, L. Liu, J. Ning, K. Lei, Y. Lu, F. Li, J. Chen, *Angew. Chem. Int. Ed.* **2018**, *57*, 9443.
[32] T. Sun, J. Xie, W. Guo, D.-S. Li, Q. Zhang, *Adv. Energy Mater.* **2020**, *10*, 1904199.
[33] A. Molina, N. Patil, E. Ventosa, M. Liras, J. Palma, R. Marcilla, *ACS Energy Lett.* **2020**, *5*, 2945.
[34] R. van der Jagt, A. Vasileiadis, H. Veldhuizen, P. Shao, X. Feng, S. Ganapathy, N. C. Habisreutinger, M. A. van der Veen, C. Wang, M. Wagemaker, S. van der Zwaag, A. Nagai, *Chem. Mater.* **2021**, *33*, 818.
[35] S. Biswas, A. Pramanik, A. Dey, S. Chattopadhyay, T. S. Pieshkov, S. Bhattacharyya, P. M. Ajayan, T. K. Maji, *Small* **2024**, *20*, 2406173.
[36] J. Sun, Y. Xu, Y. Lv, Q. Zhang, X. Zhou, *CCS Chem.* **2023**, *5*, 1259.
[37] S. Xu, Q. Zhang, *Mater. Today Energy* **2021**, *20*, 100635.
[38] M. Mahato, S. Nam, R. Tabassian, S. Oh, V. H. Nguyen, I.-K. Oh, *Adv. Funct. Mater.* **2022**, *32*, 2107442.
[39] N. Yang, Y. Gu, Y. Shan, C. Tian, L. Yang, H. Jiang, H. Liu, X. Zhu, S. Dai, *ACS Macro Lett.* **2022**, *11*, 60.
[40] E. Troschke, D. Leistenschneider, T. Rensch, S. Grätz, J. Maschita, S. Ehrling, B. Klemmed, B. V. Lotsch, A. Eychmüller, L. Borchardt, S. Kaskel, *ChemSusChem* **2020**, *13*, 3192.
[41] Y. Zheng, N. A. Khan, X. Ni, K. A. I. Zhang, Y. Shen, N. Huang, X. Y. Kong, L. Ye, *Chem. Commun.* **2023**, *59*, 6314.
[42] D. Zhu, G. Xu, M. Barnes, Y. Li, C.-P. Tseng, Z. Zhang, J.-J. Zhang, Y. Zhu, S. Khalil, M. M. Rahman, R. Verduzco, P. M. Ajayan, *Adv. Funct. Mater.* **2021**, *31*, 2100505.
[43] L. Zhou, S. Jo, M. Park, L. Fang, K. Zhang, Y. Fan, Z. Hao, Y.-M. Kang, *Adv. Energy Mater.* **2021**, *11*, 2003054.

[44] G. Zhao, H. Li, Z. Gao, L. Xu, Z. Mei, S. Cai, T. Liu, X. Yang, H. Guo, X. Sun, *Adv. Funct. Mater.* **2021**, *31*, 2101019.
[45] R. Shi, L. Liu, Y. Lu, C. Wang, Y. Li, L. Li, Z. Yan, J. Chen, *Nat. Commun.* **2020**, *11*, 178.
[46] X.-X. Luo, W.-H. Li, H.-J. Liang, H.-X. Zhang, K.-D. Du, X.-T. Wang, X.-F. Liu, J.-P. Zhang, X.-L. Wu, *Angew. Chem. Int. Ed.* **2022**, *61*, e202117661.
[47] H. Gao, Q. Zhu, A. R. Neale, M. Bahri, X. Wang, H. Yang, L. Liu, R. Clowes, N. D. Browning, R. S. Sprick, M. A. Little, L. J. Hardwick, A. I. Cooper, *Adv. Energy Mater.* **2021**, *11*, 2101880.
[48] B. Sun, J. Liu, A. Cao, W. Song, D. Wang, *Chem. Commun.* **2017**, *53*, 6303.
[49] G. Wang, N. Chandrasekhar, B. P. Biswal, D. Becker, S. Paasch, E. Brunner, M. Addicoat, M. Yu, R. Berger, X. Feng, *Adv. Mater.* **2019**, *31*, 1901478.
[50] X. Yang, C. Lin, D. Han, G. Li, C. Huang, J. Liu, X. Wu, L. Zhai, L. Mi, *J. Mater. Chem. A* **2022**, *10*, 3989.
[51] Y. Liang, C. Luo, F. Wang, S. Hou, S.-C. Liou, T. Qing, Q. Li, J. Zheng, C. Cui, C. Wang, *Adv. Energy Mater.* **2019**, *9*, 1802986.
[52] X. Li, A. Lushington, Q. Sun, W. Xiao, J. Liu, B. Wang, Y. Ye, K. Nie, Y. Hu, Q. Xiao, R. Li, J. Guo, T.-K. Sham, X. Sun, *Nano Lett.* **2016**, *16*, 3545.
[53] J. Xu, J. Zhang, T. P. Pollard, Q. Li, S. Tan, S. Hou, H. Wan, F. Chen, H. He, E. Hu, K. Xu, X.-Q. Yang, O. Borodin, C. Wang, *Nature* **2023**, *614*, 694.
[54] K. B. Hueso, M. Armand, T. Rojo, *Energy Environ. Sci.* **2013**, *6*, 734.
[55] Y. Zhou, X. Zhang, Y. Liu, X. Xie, X. Rui, X. Zhang, Y. Feng, X. Zhang, Y. Yu, K. Huang, *Small* **2020**, *16*, 1906669.
[56] C. Wang, D. Du, M. Song, Y. Wang, F. Li, *Adv. Energy Mater.* **2019**, *9*, 1900022.
[57] A. Dey, S. Chakraborty, A. Singh, F. A. Rahimi, S. Biswas, T. Mandal, T. K. Maji, *Angew. Chem., Int. Ed.* **2024**, *n/a*, e202403093.
[58] B. Díaz de Greñu, J. Torres, J. García-González, S. Muñoz-Pina, R. de los Reyes, A. M. Costero, P. Amorós, J. V. Ros-Lis, *ChemSusChem* **2021**, *14*, 208.
[59] X. Chen, Q. Dang, R. Sa, L. Li, L. Li, J. Bi, Z. Zhang, J. Long, Y. Yu, Z. Zou, *Chem. Sci.* **2020**, *11*, 6915.
[60] X. Zhu, S. An, Y. Liu, J. Hu, H. Liu, C. Tian, S. Dai, X. Yang, H. Wang, C. W. Abney, S. Dai, *AIChE J.* **2017**, *63*, 3470.
[61] L. Ai, C. Zhang, F. Liao, Y. Wang, M. Li, L. Meng, J. Jiang, *J. Hazard. Mater.* **2011**, *198*, 282.
[62] X. He, X. Xu, G. Bo, Y. Yan, *RSC Adv.* **2020**, *10*, 2180.
[63] J. Wang, J. Polleux, J. Lim, B. Dunn, *J. Phys. Chem. C* **2007**, *111*, 14925.
[64] A. Pramanik, P. L. Mahapatra, R. Tromer, J. Xu, G. Costin, C. Li, S. Saju, S. Alhashim, K. Pandey, A. Srivastava, R. Vajtai, D. S. Galvao, C. S. Tiwary, P. M. Ajayan, *ACS Appl. Mater. Interfaces* **2024**, *16*, 2417.
[65] J.-L. Xia, D. Yan, L.-P. Guo, X.-L. Dong, W.-C. Li, A.-H. Lu, *Adv. Mater.* **2020**, *32*, 2000447.
[66] J. Duan, W. Wang, D. Zou, J. Liu, N. Li, J. Weng, L.-p. Xu, Y. Guan, Y. Zhang, P. Zhou, *ACS Appl. Mater. Interfaces* **2022**, *14*, 31234.
[67] Z. Guo, S. Yang, M. Liu, Q. Xu, G. Zeng, *EcoEnergy* **2024**, *2*, 192.
[68] M. K. Shehab, K. S. Weeraratne, O. M. El-Kadri, V. K. Yadavalli, H. M. El-Kaderi, *Macromol. Rapid Commun.* **2023**, *44*, 2200782.
[69] G. Kresse, J. Furthmüller, *Phys. Rev. B* **1996**, *54*, 11169.
[70] G. Kresse, J. Furthmüller, *Comput. Mater. Sci.* **1996**, *6*, 15.
[71] J. Sun, A. Ruzsinszky, J. P. Perdew, *Phys. Rev. Lett.* **2015**, *115*, 036402.
[72] J. S. Murray, P. Politzer, *WIREs Comput. Mol. Sci.* **2011**, *1*, 153.

Manuscript received: October 28, 2024
Revised manuscript received: January 17, 2025
Version of record online: ■■, ■■